CHEMISTRY OF MATERIALS

pubs.acs.org/cm

Article

Bioinspired Compartmentalization Strategy for Coating Polymers with Self-Organized Prismatic Films

Zheng-Zheng Li, Ming Li, Yu-xuan Feng, Zhisen Zhang,* Yue-E Wen, Qi-Qi Huang, Zihao Lu, Hua Bai, Hai-Long Wang, Bin-Bin Xu, Helmut Cölfen, Peter Fratzl,* Shahrouz Amini,* and Yuan Jiang*

Cite This: *Chem. Mater.* 2021, 33, 9240–9251

Read Online

ACCESS | Metrics & More | Article Recommendations | Supporting Information

ABSTRACT: Biomineralization provides load-bearing and protective functions to living organisms by reinforcing soft tissues. Translation of biomineralization principles to materials science in a controlled and self-organized fashion is highly desirable but challenging. A major lesson from natural systems is that crystallization may be controlled by compartmentalization and templating. Here, we develop a crystallization technique based on graphene oxide-mediated compartmentalization and on templating prismatic growth of calcite nanocoatings *via* control of ionic diffusivity into the microcompartments, which results in a multistage, self-organized crystallization and represents an effective strategy for providing continuous nanocoatings and enhancing the tribological performance of polymeric surfaces under contact stresses. The present research offers a bottom-up approach of using very basic biomineralization principles for the protection of polymeric surfaces, which are of interest for biomedical applications and the fabrication of high-performance functional materials in a sustainable manner.

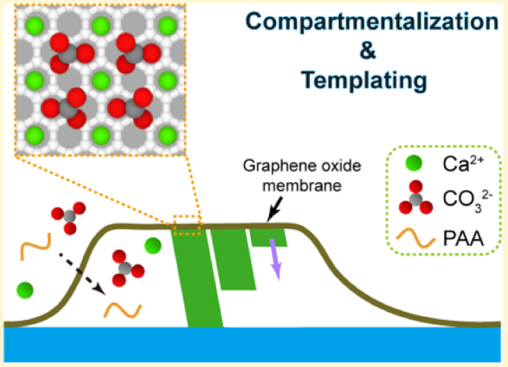

INTRODUCTION

Mechanical protection—resistance to contact stresses imposed by external mechanical stimuli—has been a central need in the survival of a diverse group of living organisms from minute Arthropoda to gigantic Mammals.[1−3] Mechanistically, materials that possess higher hardness and stiffness exhibit greater resistance to residual deformations and contact damages (*e.g.*, penetration, wear, and abrasion), a determining factor for the tribological performance of materials.[4] Hence, the demand for mechanical protection can be addressed by reinforcing the contact regions. Remarkably, tissue hardening has been the evolutionary solution of nature to support this demand and promote the tribological performance and protective function of biological tissues.[5−7] Biomineralization, by far, has been the greatest solution for the enhancement of tribological characteristics of biological materials in which the presence of mineral blocks improves the hardness and elastic modulus of the organic tissues by more than 1 order of magnitude.[7] Tissue hardening comes with its own cost associated with the required additional formation process, imposing limitations on flexibility and often incrementing the tissues' brittleness. Consequently, materials' hardening often forms at the contact areas rather than in the entire soft tissues, shaping a protective shield. Biological hard shields have been frequently deployed at the exterior layer (contact region) of a variety of mechanically demanding tissues such as biting mouthparts,[8] appendages,[9,10] and cuticle of invertebrates[11,12] and dermal armor of vertebrates,[13,14] which are prone to high contact stresses and tribological damages. Many exterior layers, exemplified by enamels in vertebrate teeth[15] and prismatic layers in invertebrate shells,[16] are composed of prisms of different compositions, sizes, and elongation degrees oriented normal to the surface.

Bioinspiration of prismatic coatings with tribological performance and deploying them for biomedical applications has been a desired objective for materials scientists.[17−20] Yet, forming continuous prismatic minerals in a controlled and self-organized fashion and compatible with different substrates remains a challenging target. Current synthetic routes to prismatic coatings are based on seeded mineralization,[21] where the templating effect between polymeric matrices and mineralized layers is indispensable.[18,22] Though the prismatic mineral can exhibit the comparable mechanical performance with their biogenic counterparts,[21] the selection pool of polymer matrices is limited to few hydrophilic candidates. By contrast, biomineralization of mollusk shells proceeds in the sealed microcompartments called extrapallial space, wherein the sophisticated microenvironment guarantees the sequential

Received: August 23, 2021
Revised: November 10, 2021
Published: November 25, 2021

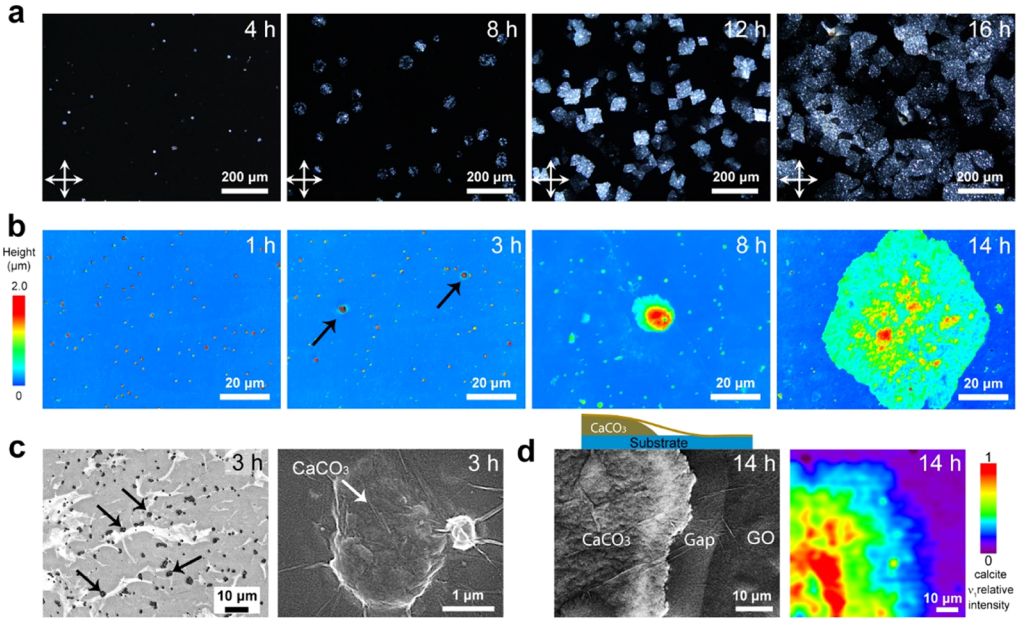

Figure 1. Formation kinetics of mineralized nanocoatings on GO-covered PVC/chitosan substrates. (a) Time-resolved POM images showing the growth kinetics of the $CaCO_3$ nanocoatings deposited on GO-covered PVC substrates. (b) CLSM images (height view) showing time-resolved topographic information of growing $CaCO_3$ nanocoatings on GO-covered chitosan substrates (Supporting Information Figure S2a–d). (c) CLSM (laser view) and SEM images showing the structure of particulate seeds on GO-covered PVC/chitosan substrates. (d) SEM image and Raman map showing the structural information of growing nanocoatings on GO-covered PVC/chitosan substrates. Raman spectroscopic image of the ν_1 vibrational band of carbonate showing a transition between a typical growing domain of the $CaCO_3$ nanocoating and the superimposed GO layers. See supporting Raman spectroscopic information in Supporting Information Figure S4a–c.

deposition of prismatic and nacreous mineralized layers.[16,23] This biomineralization scenario highlights the multiple roles of the interior mantle tissue—a skin-like tissue beneath the mollusk's body wall, which not only controls the diffusion of reactants in microcompartments for the establishment of a dynamic microenvironment but templates the deposition of the continuous, prismatic layer on which prisms continued growing to full thickness. In mimics of biogenic microcompartments, confined physical agents exemplified by narrow space,[24] porous solids,[25] and microdroplets[26] were introduced to promote the occurrence of complex structures *via* self-organized mineralization. Nevertheless, none exhibits morphological similarity to biominerals as such physical confined space lacks ionic permeation capability and cannot maintain constant supersaturation levels in the course of mineralization. It is therefore anticipated that the establishment of a bioinspired route based on compartmentalization can eventually integrate prismatic layers with variant polymeric surfaces, endowing the latter with superior tribological characteristics. The success in principle can reward us with reinforced polymeric surfaces, which is of great interest for biomedical applications.

In the current work, we deployed a bioinspired compartmentalization to develop an alternative biomineralization route to forming and integrating continuous crystalline prismatic nanocoatings with polymeric substrates, resulting in a pronounced enhancement in the tribological performance of the polymeric substrates. Graphene oxide (GO)-mediated compartmentalization set up a self-organized microenvironment, wherein the selective permeation of reactants guaranteed the formation of continuous nanocoatings. Moreover, the superimposed GO layer also functioned as a surface of heterogeneous nucleation, facilitating the formation of prismatic nanocoatings with vertical orientational preference. GO-mediated compartmentalization afforded us an emerging opportunity to establish a general approach of integrating prismatic nanocoatings with variant polymeric surfaces and therefore of using the fundamental biomineralization principle of the reinforcement of soft tissues for the protection of polymeric surfaces in a sustainable manner.

RESULTS

Formation of Prismatic Nanocoatings. Multiple time-resolved microscopic tools were deployed to disclose the formation and development of nanocoatings on GO-covered polyvinyl chloride (PVC)/chitosan substrates (Supporting Information Figure S1a,b), aiming for elucidating a clear spatiotemporal evolution in the course of crystallization. Time-resolved polarized optical microscopic (POM) images illustrated the occurrence of sporadic polydomains on GO-covered PVC, followed by their lateral expansion to the confluence at the millimeter length scale (Figure 1a). The varied birefringent contrast of each growing polydomain denoted their random lateral orientation. Furthermore, time-resolved confocal laser scanning microscopy (CLSM) provided a detailed structural progress at the microscopic length scale. The CLSM results obtained from GO-covered chitosan confirmed that the initially formed seeds were several micrometers in height, which was notably higher than that of fully grown nanocoatings (Figure 1b and Supporting Information Figure S2a–d). Moreover, the formation of seeds in the GO-covered chitosan microcompartments was disclosed by the appearance of GO wrinkles atop in an exemplary scanning electron microscopic (SEM) image (Figure 1c—SEM). Therefore, the enrichment of Ca^{2+} by the localization of the superimposed GO layers[27] could lead to high supersaturation levels in the narrow space between the superimposed GO layer and the polymeric substrates, and consequently, self-organized crystallization caused the local occurrence of 3D seeds (Figure

https://doi.org/10.1021/acs.chemmater.1c02868
Chem. Mater. 2021, 33, 9240–9251

1c). These seeds were crystalline and calcitic in polymorphs, which were revealed by the strong birefringent contrast under polarized light (Figure 1a—4 h) and the corresponding calcite Raman bands (Supporting Information Figure S3).

The GO-covered PVC/chitosan substrates next compartmentalized the lateral, concentric expansion of the domains, each of which was centered by a 3D seed (Figure 1b). The growth front of each domain showed a constant value of thickness in the course of lateral expansion (Supporting Information Figure S2c,d), and the collected Raman map illustrated the calcitic character of the growth front of an exemplary domain (Figure 1d—Raman map and Supporting Information Figure S4a−c). Notably, we found a gap of about 10 μm in width between the edge of the superimposed GO layer and the growth front of a growing domain underneath (Figure 1d—SEM), where the fast permeation of Ca^{2+} through the superimposed GO layer[28] should be critical to the continuous spread of growing domains. With time, the 3D seeds continued flattening until their height was comparable to that of growing nanocoatings (Supporting Information Figure S2b−d). The tight contact of the GO layer on continuous nanocoatings blocked the further thickening of the continuous nanocoatings. Comparably, the coverage of Marsh's membranes is responsible for the termination of the thickening of prismatic layers in the formation of mollusk shells.[29]

Characterization of $CaCO_3$ Nanocoatings. The mineralization led to the mineral deposition on GO-covered PVC/chitosan substrates eventually (Figure 2a−d). The structural continuity and polycrystalline texture of both nanocoatings on polymeric substrates were evidenced by POM (Figure 2a,c), and cross-sectional SEM images (Figure 2b,d) provided unambiguous evidence that the $CaCO_3$ nanocoatings were uniformly sandwiched by the superimposed GO layer and polymeric substrates. Transmission electron microscopic (TEM) images associated with selective area electron diffraction patterns demonstrated that the selected nanodomains were characteristic of single crystalline-like structures with the (1 0 4) facet being in parallel to the substrate (Figure 3a,b). These TEM results, together with the dominance of the (1 0 4) peak in the X-ray diffraction (XRD) pattern (Supporting Information Figure S5), revealed that the nanocoatings were prismatic in ultrastructural form and approximately oriented in the vertical direction. A crystallization protocol proceeding on pristine PVC led to the deposition of sporadic microcrystals instead (Supporting Information Figure S6), ascribed to the weak binding affinity between hydrated Ca^{2+} and PVC that caused the large magnitude of the diffusive barrier for reacting cations to reach the polymeric surface.[30,31] This comparison experiment confirmed that the superimposed GO layer played a pivotal role in the formation of continuous nanocoatings.

As a proof of concept, GO-mediated compartmentalization successfully delivered continuous $CaCO_3$ nanocoatings on polyethylene films, patterned chitosan surfaces, and silk fibroin and Nylon 66 fibers evidenced by the intense band (ν_1) of calcite Raman spectrum (Supporting Information Figure S7a−c), which suggested that compartmentalization could become a general approach for growing $CaCO_3$ nanocoatings on variant polymeric substrates. Moreover, it is worth noting that the presence of the PAA constituents was also indispensable for the formation of uniform nanocoatings as a comparison experiment showed that crystallization in its absence led to the deposition of individual rhombohedral crystals (Supporting Information Figure S8a,b), in agreement with a previous finding.[32] To our

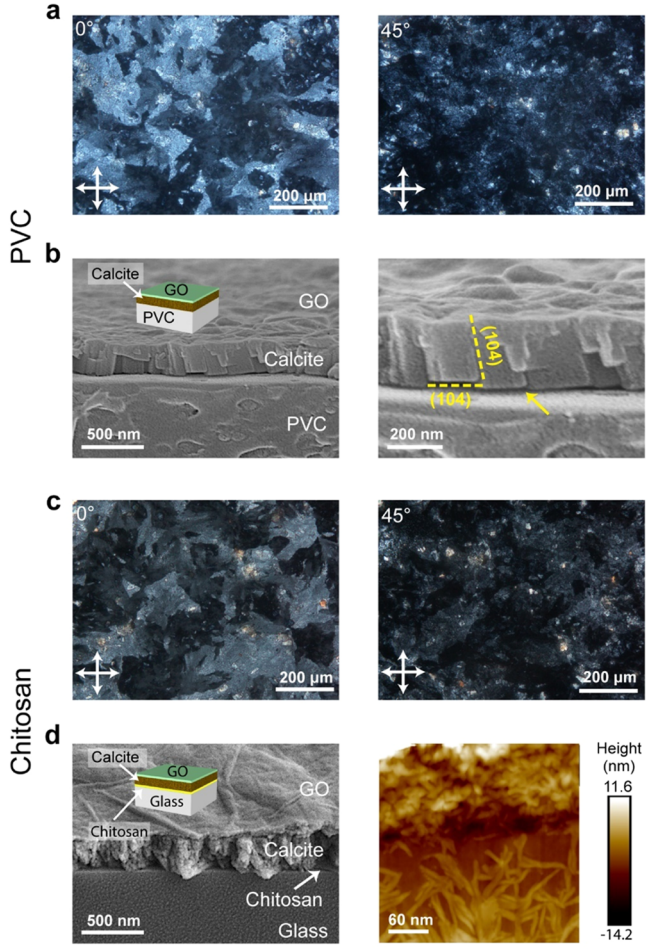

Figure 2. Characterization of the $CaCO_3$ nanocoatings deposited on GO-covered PVC/chitosan substrates. (a,c) POM images of $CaCO_3$ nanocoatings deposited on GO adsorbed PVC (a) and chitosan (c) substrates. (b) Cross-sectional SEM images of the $CaCO_3$ nanocoatings deposited on PVC reveal a prismatic structure of $CaCO_3$ films with a clear rhombohedral morphology. The yellow arrow denotes the gap between $CaCO_3$ nanocoatings and PVC substrates. (d) Cross-sectional SEM (left) and AFM (right) of the $CaCO_3$ nanocoatings deposited on chitosan disclose the formation of $CaCO_3$ minerals with a granular architecture.

knowledge, no superimposed GO layer has been used as microcompartments for the formation of crystalline films, though individual GO nanosheets functioned as colloidal additives for the morphosyntheses of $CaCO_3$ crystals.[33]

GO-covered PVC/chitosan substrates led to the distinct ultrastructural forms of the prismatic nanocoatings. Nanocoatings on GO-covered PVC were composed of rhombohedral nanoprisms, where single crystalline-like nanoprisms were tightly packed and roughly oriented with the exposure of low-energy, calcitic (1 0 4) planes (Figure 2b). The interface between adjacent nanoprisms was filled with a thin layer of amorphous-like structures, which could be assumedly composed of $CaCO_3$−PAA constituents (Figure 3a). The polymer-rich constituents were expelled from growing nanoprisms in the course of crystallization[34,35] and, in principle, could function as interprismatic layers that gave rise to the fracture resistance of the prismatic nanocoatings.[36] In contrast, the nanocoatings deposited on GO-covered chitosan were composed of granular, nanocrystalline structures (Figures 2d and 3b), which was reminiscent of the nanoparticle accretion pathway[37]—a non-

https://doi.org/10.1021/acs.chemmater.1c02868
Chem. Mater. 2021, 33, 9240−9251

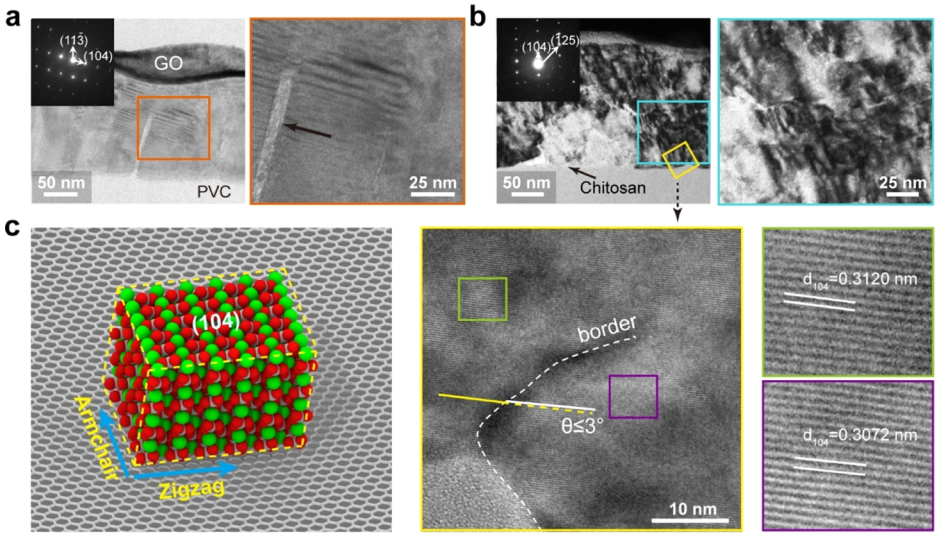

Figure 3. Ultrastructural and orientational information of the prismatic nanocoatings. (a,b) Bright-field TEM images and related SAED patterns of the $CaCO_3$ nanocoatings deposited on PVC (a) and chitosan (b) substrates showing the preferred vertical orientation of the prismatic $CaCO_3$. In image (b), HR-TEM images show the orientation of the nanocrystalline grains, where coincident lines indicate the presence of a small-angled mismatch (θ) of about 3° between adjacent crystalline nanodomains. Black arrows in the HR-TEM image denote the interface between adjacent nanocrystals, and the squares in both TEM images illustrate the domains for collecting SAED patterns. (c) 3D illustration showing a structural match between the calcitic (1 0 4) facet and the graphene plane.

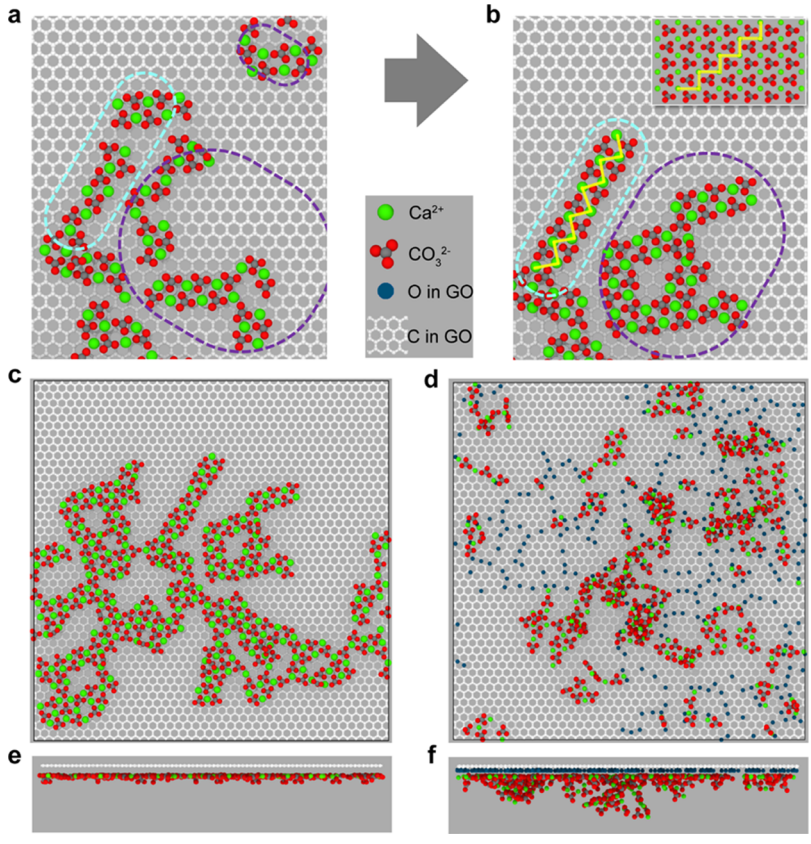

Figure 4. Mechanism of calcite formation on GO and graphene surfaces by MD simulations. (a,b) Incorporation of small Ca^{2+}/CO_3^{2-} clusters into a large domain on the graphene surface, where both images show the moments before (a) and after (b) incorporation. The calcite-like clusters are highlighted by dashed cyan-purple circles. The atomic structure of the calcite (1 0 4) face (top view) is inserted in image (b), typical arrangement of Ca^{2+} of the calcite (1 0 4) face in an exemplary cluster is highlighted with a zigzag-shaped yellow line. (c–f) Snapshots of Ca^{2+}/CO_3^{2-} clusters formed on graphene [images (c,e) are top- and side-view, respectively] and GO [images (d,f) are top- and side-view, respectively] surfaces by MD simulation. Water molecules and hydrogen atoms are not shown for clarity.

classical crystallization pathway proceeding in high supersaturation levels.[38] The ultrastructural difference in both nanocoatings can be primarily ascribed to the distinct thickness of the superimposed GO layers on PVC/chitosan substrates,

https://doi.org/10.1021/acs.chemmater.1c02868
Chem. Mater. 2021, 33, 9240−9251

suggesting that the relatively small thicknesses of the superimposed GO layers on PVC (Supporting Information Figure S1c) facilitate the diffusion of Ca^{2+} in microcompartments and promote the stepwise growth of nanoprisms. By contrast, the relatively thick GO layers on chitosan (Supporting Information Figure S1c) could increase the difficulty of Ca^{2+} diffusivity dramatically, which eventually caused the retardancy of crystallization. Moreover, the chitosan substrate rich in hydrogen bonding interactions in principle has an impact on the enrichment of calcium cations in microcompartments that could cause the increase of the local supersaturation levels for the formation of nanocoatings granular in nature. By contrast, PVC lacks apparent molecular interactions with reactants, and the crystallization behaviors in GO-covered PVC should be mainly guided by the superimposed GO layers. Therefore, both the distinct thickness of the superimposed GO layers and the chemistry of the polymeric surfaces caused the morphological difference of both nanocoatings.

Additionally, the revealed small-angled mismatch of 1−3° between nanocrystalline grains in the nanocoatings on GO-covered chitosan [Figure 3b—high-resolution TEM (HR-TEM)] confirmed that coherent nanocrystals were not strictly crystallographically ordered, and its appearance was assumedly attributed to the imperfect accretion of nanoparticles at extreme supersaturation levels.[39,40] It is worth noting that small-angled misoriented interfaces in coherent nanocrystals can give rise to crack deflection—a universal toughening mechanism for biominerals and nanostructured hybrids at the nanoscale.[41,42] The promotion of calcitic growth on the superimposed GO layers can be attributed to the complementary structural match between the sp^2 domain of GO nanosheets and the calcitic (1 0 4) facet (Figure 3c). Similarly, the formation of crystalline films in the polymeric matrices has been reported by Kato and co-workers, where the structural match between polyvinyl alcohol and aragonite $CaCO_3$ led to the formation of needle-like crystals underneath.[43]

Mechanistic Understanding of Templating and Compartmentalization. In the nanocoatings deposited on GO-covered PVC, relatively small rhombohedral nanocrystals were closely associated with the superimposed GO layer (Figure 2b—SEM). This result suggested that the crystallization could start from the GO surface instead of the polymeric substrates. Prior to lateral growth, the selective nucleation of $CaCO_3$ on GO can be ascribed to the amphiphilic nature of GO owing to its spatial delocalization of sp^2 (relatively hydrophobic) and sp^3 (relatively hydrophilic) domains.[44] Molecular dynamics (MD) simulation was employed to explore the mechanism of calcite formation on GO and graphene surfaces (Supporting Information Figure S9). The relatively weak cation−π interaction[45] enriched Ca^{2+}/CO_3^{2-} ions on the graphene surface, which led to the in-plane movement of Ca^{2+}/CO_3^{2-} clusters, and consequently, an ordered domain was formed *via* the incorporation of small Ca^{2+}/CO_3^{2-} clusters, exhibiting a calcite-like structure (Figure 4a,b dashed circles). Based on the MD simulation results, it is reasonable to infer that the delocalized hydrophobic domain of GO nanosheets should exhibit a high affinity to the calcite (1 0 4) facet owing to the geometric match (Figure 4c,e), which was in line with the experimental results [Figure 3a,b—selected area electron diffraction (SAED) patterns]. By contrast, the MD simulation showed that the Ca^{2+} and CO_3^{2-} ions tended to form 3D disordered clusters on the GO surface (Figure 4d,f), and moreover, these Ca^{2+}/CO_3^{2-} clusters were difficult to move freely on the GO surface ascribed to their strong binding affinity with the GO substrate. The presence of oxidized groups (such as hydroxyl and epoxy ones) near the hydrophobic domain increased the binding affinity of the substrate to Ca^{2+}/CO_3^{2-} ions, accelerating the adsorption process of Ca^{2+}/CO_3^{2-} ions to its surface.[44] Hence, the relatively hydrophilic domain on the margin of GO nanosheets was responsible for the enrichment of Ca^{2+}/CO_3^{2-} clusters, and the relatively hydrophobic domain close to the margins became the favored positions for $CaCO_3$ crystallization. Experimentally, the nucleation proceeding in the marginal domains of superimposed GO layers was disclosed in a CLSM image (Figure 1c), which verifies the validity of the MD simulation. The preferential nucleation on the superimposed GO layer was reminiscent of periostracal mineralization, where the thin, prismatic layer in direct contact with the periostracum was formed on the inner surface of the mantle tissue atop.[46]

Besides the templating effect, GO-mediated compartmentalization should exhibit an impact on the morphogenesis *via* the selective permeation of cations in microcompartments. A series of comparison experiments were therefore deployed to disclose the impact of the cationic diffusivity of GO on the structural outcome of the mineralized products. Chemical reduction selectively removed hydroxyl and epoxy groups in the hydrophilic framework of GO, resulting in the formation of reduced GO (rGO) carrying relatively large diffusive barriers of Ca^{2+} permeation.[44] In a comparison test, rGO-covered PVC led to the formation of discontinuous $CaCO_3$ polydomains 1.04 ± 0.05 μm (N = 10) in thickness (Supporting Information Figure S10a,b), which verifies the important role of the cationic permeability of the superimposed layers. In addition to hydroxyl and epoxy groups, carboxyl groups in the sp^3 domains of GO also played a key role in the diffusion of Ca^{2+} into microcompartments for crystallization purposes. In the course of $CaCO_3$ crystallization, the abrupt addition of transition metal cations such as Cu^{2+}, Ni^{2+}, and Zn^{2+} terminated the continuous growth of crystalline $CaCO_3$ polydomains (Supporting Information Figure S11a−c) because the transportation of Ca^{2+} through the superimposed GO layer was blocked owing to the formation of coordinate complexes between the d electrons of the transition metal cations and the carboxyl groups of GO.[47] Moreover, the permeability of metal cations is pivotal for their diffusion through the superimposed GO layers. In a comparison mineralization, the relatively fast permeation of hydrated Ba^{2+} led to the deposition of discontinuous $BaCO_3$ nanocoatings 659.9 ± 60.1 nm (N = 10) in thickness on GO-covered PVC (Supporting Information Figure S12), which was attributed to the relatively large size of Ba^{2+} that led to a weaker hydration layer and weaker interactions with the oxidation groups of GO.[47,48] These results verify that the compartmentalization characterized by the selective permeation of metal cations through the GO membranes gave rise to the formation of continuous crystalline nanocoatings. Though previous studies have used GO in the morphogenesis of $CaCO_3$ minerals,[33,49] none has taken advantage of the cationic permeability of GO for the establishment of reaction-diffusion systems in the delivery of self-organized $CaCO_3$ nanocoatings.

Tribological Characteristics of Prismatic Nanocoatings. The tribological performance of thin coatings, such as resistance to wear and scratch damages, is determined by parameters such as surface roughness, mechanical properties of coating and substrate, cohesive strength of the coating, and coating-substrate interfacial adhesion. To quantify the tribological performance of the prismatic nanocoatings and evaluate the stability of the coating-substrate system, we conducted a

https://doi.org/10.1021/acs.chemmater.1c02868
Chem. Mater. 2021, 33, 9240−9251

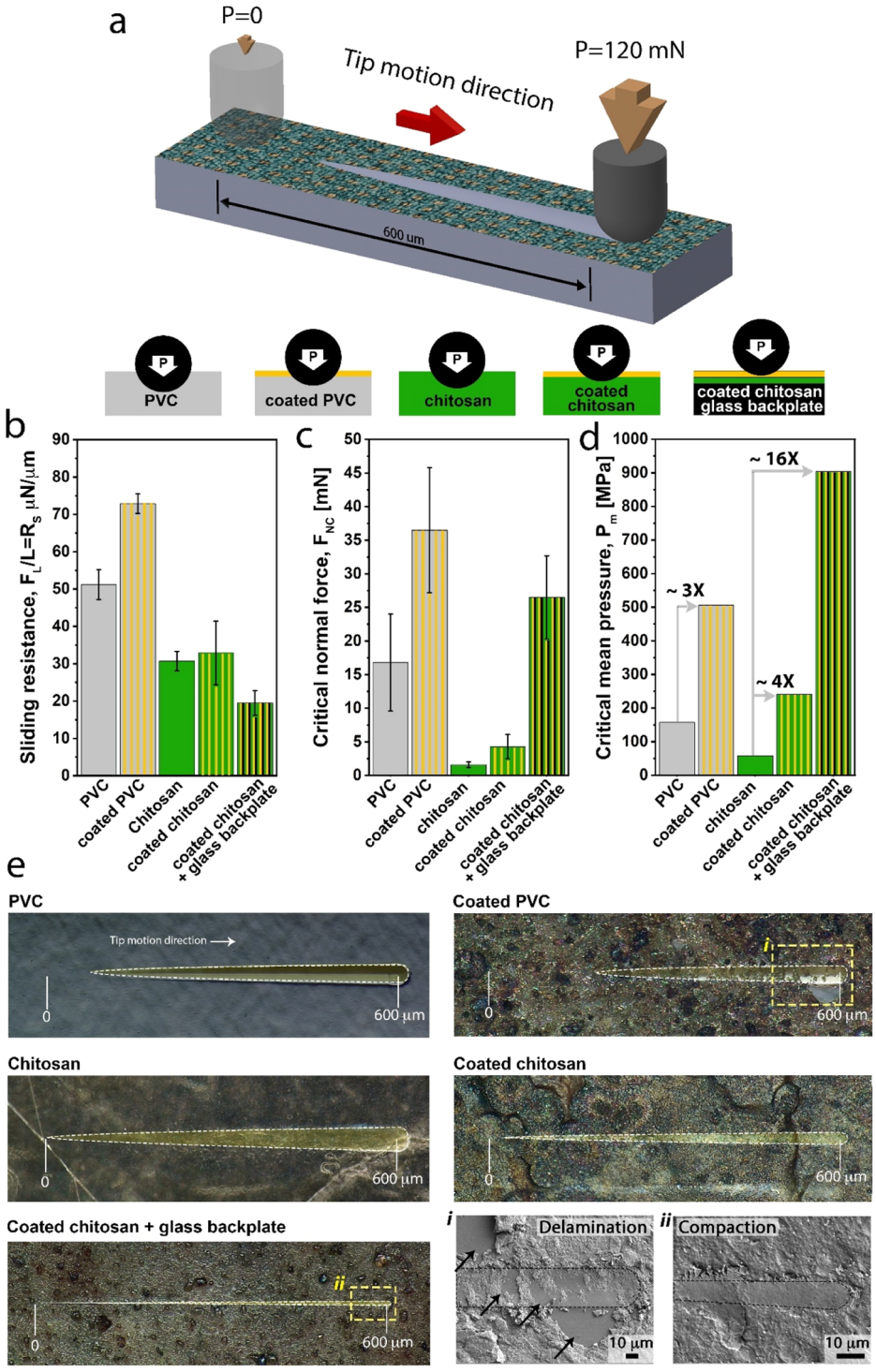

Figure 5. Tribological performance of the nanocoatings and corresponding polymeric substrates. (a) Schematic model of the scratch test showing a gradual increase in the normal load along the scratch track. (b) Sliding resistance, (c) critical normal forces, and (d) critical mean pressure of the samples showing the enhancement in the mechanical response of the polymeric samples after nanocoatings. Data are shown as mean ± S.D. ($N = 6$). (e) Post-scratch optical and electron microscopy micrographs captured from the scratch tracks showing the different damage modes. The delamination damages in and around the scratch tracks in coated PVC sample reveal a weak adhesion between the PVC and crystalline nanocoatings (e-i and Supporting Information Figure S14b). In contrast, cohesive micro-cracking and proper adhesion to the substrate in coated chitosan samples (e-ii and Supporting Information Figure S14c) reveal the promising tribological performance of the sample.

series of ramped load micro-scratch tests[50] (Figure 5a), wherein the surface of the sample was exposed to an incremental normal load (F_N) over a lateral displacement (L). The recorded lateral forces (F_L) along the scratch track revealed a higher sliding resistance (F_L/L) in the coated samples in comparison to the polymeric substrate (Figure 5b). This increment can be mainly attributed to the higher surface roughness and structural texture of the prismatic nanocoating. The post-scratch optical micrographs (Figure 5e) demonstrated a lower penetration depth in the coated samples as evidenced by the narrowing of the residual

https://doi.org/10.1021/acs.chemmater.1c02868
Chem. Mater. 2021, 33, 9240−9251

scratch tracks (Figure 5e, areas highlighted in yellow), which can be correlated to the higher elastic moduli of the coated samples (Supporting Information Figure S13).

Remarkably, the critical normal force (F_{NC})—a force required to induce the first residual deformation on the sample surface—has been significantly improved for the coated samples (Figure 5c). This means that despite a decrease in the contact area and consequently an increase in contact stress, the mineralized nanocoating advances the resistance to scratch. This enhancement in tribological performance was clearly evidenced by the calculated critical mean pressure (P_m),[51] which is required to induce inelastic damages as a result of a scratch (Figure 5d). Despite the similarities in the enhancement of tribological properties of the coated samples, our post-scratch microscopic investigation on the coated samples revealed that applied stresses result in two different damage mechanisms, namely, delamination and compaction in coated PVC and coated chitosan samples, respectively (Supporting Information Figure S14a). Yet, to confirm the compaction mechanism in the coated chitosan sample, we used a coated chitosan sample with a glass backplate in which the rigidity of the glass backplate confines the strain, resulting in a drastic increase in contact stress.

A ∼16-fold increase in the critical normal force and pressure in coated chitosan with a glass backplate sample compared to non-coated chitosan confirmed our proposed compaction mechanism and suggested that the dominant damage mode in prismatic coatings should be related to a strain mismatch between the substrate and coating rather than a cohesive failure. This hypothesis was examined by our in-depth post-scratch microscopic investigation on the scratch tracks, providing clear insights into induced damages in the mineral coating and coating-substrate systems. Two distinct damage mechanisms in the coated samples (Figure 5e—SEM and Supporting Information Figure S14b,c) revealed that while the scratch tracks in coated chitosan samples with a glass backplate only showed cohesive micro-cracking [Figure 5e—SEM (right) and Supporting Information Figure S14c], the coated PVC sample contained adhesion failures and delamination supported by the exposure of the PVC substrate [Figure 5e—SEM (left) and Supporting Information Figure S14b]. Furthermore, the far-field delamination in the coated PVC sample confirmed that a weak adhesion between the coating and PVC was replaced by a strong adhesion between the chitosan and prismatic coatings.

DISCUSSION

Unlike the GO-mediated compartmentalization introduced herein, the existing confining agents such as patterned surfaces,[52] liquid droplets,[26] pores,[25] and membranes[53] lack the capability of fast, selective ionic permeation. Though reacting ions can diffuse freely in physically confined space, the crystallization depletes reacting reagents quickly, proceeds under near-equilibrium conditions, and finally leads to isolated microcrystals instead of continuous (thin) films.[54] By contrast, superimposed GO layers compartmentalize and template the formation of prismatic nanocoatings, determining the rate, location, and face selectivity of $CaCO_3$ nucleation by taking advantage of the crystallographic structure, amphiphilic nature, and shape-anisotropy of individual GO nanosheets and their layered assembly mode. This coupled effect exhibits profound similarities to the initial stages of mollusk shells[16,46] and coccolith[55] biogenesis in terms of localization and structural control.

Compartmentalization ensured the integration of prismatic nanocoatings on varied polymeric substrates—regardless of hydrophilic or hydrophobic—directly from an aqueous phase without the involvement of harsh treatments and chemicals. Additionally, the prismatic $CaCO_3$ nanocoating can be removed from the polymeric substrates simply by acid washing. Therefore, this emerging approach shows a considerable advantage compared with current liquid deposition processes, including sol−gel deposition and layer-by-layer assembly. As a comparison, sol−gel approaches involve the use of organic precursor phases and evaporation of volatile constituents[56] and the granular thin films obtained, irrelevant of their amorphous or crystalline nature, show moderate hardening performance, while layer-by-layer deposition contains tedious circulation in polyelectrolyte solutions and counter-charged colloidal dispersions.[57]

The biomineralization strategy based on compartmentalization and templating was used to develop a crystallization approach for reinforcing multiple polymeric substrates with prismatic nanocoatings. Moreover, the superimposed GO layers—in mimics of the mantle tissue in mollusk animals—can be characterized, and there is the potential to systematically change structural parameters such as particle size, surface charge, and organization to study the impact of dynamic reaction-diffusion systems on the ultrastructural forms. Hence, compartmentalization-mediated crystallization can become a rational, self-organized approach for the solution-based deposition of crystalline thin films on variant polymeric substrates with the availability of precise ultrastructural control, where subsequent characterization facilitates the comprehensive understanding of the influence of compartmentalization on the formation-structure−property of these complex architectures. This bioinspired strategy introduced herein can be extended for the integration of engineering and functional nanocoatings on polymer materials for the fabrication of sustainable materials with the reconciliation of multiple functions. Plastic pollution undoubtedly is becoming one of the major challenges in the coming decades and centuries. The strategy proposed here has been evolved by nature dating back to hundreds of million years ago and can be used for the enhancement of the durability of plastic materials and thus increased time of usage in a sustainable manner in the near future.

EXPERIMENTAL SECTION

Preparation of the GO Dispersions. GO was prepared from natural graphite powder (Sigma-Aldrich, ∼325 mesh particle size, ≥99%) by a modified Hummers method[58] and purified by dialysis (dialysis membrane information: Spectra/Por 2, MWCO 8000−14,000) for 2 weeks to remove the impurities. The solid content of GO was 10 mg mL^{-1} with the gravimetric method. Atomic force microscopy (AFM) was used to evaluate the size distribution of GO nanosheets (Supporting Information Figure S15a). X-ray photoelectron spectroscopy (XPS) was used for the chemical analysis of GO nanosheets (Supporting Information Figure S15b).

Preparation of Polymeric Substrates. Chitosan thin films on glass substrates were prepared as follows. A volume of 30 μL 1 wt % chitosan-acetic acid solution (chitosan: M_w = 3.0 × 10^5 g mol^{-1}, viscosity: 800−2000 cP, deacetylation degree: 95%, Sigma-Aldrich; acetic acid: ≥99.8%, analytical standard) was dropped on a cover glass (10 mm × 10 mm, pretreated with Piranha solution), followed by a spin-coating process with a spin rate of 5000 rpm for 45 s. Piranha solution was made fresh in glassware before each use. The solution was prepared in a fume hood, and the operator wore gloves, a lab coat, and safety goggles. Free-standing chitosan films were prepared as follows. The degassed (ultrasonication) chitosan acetic acid solution (1 wt %)

https://doi.org/10.1021/acs.chemmater.1c02868
Chem. Mater. 2021, 33, 9240−9251

was cast onto a glass plate to ensure solution thickness of about 1 mm, and the wet film together with the plate was exposed to air in ambient condition for 12 h. After that, the glass plate was immersed in a solution of 4 wt % sodium hydroxide (reagent grade, ≥98%, anhydrous pellets) for 10 min. The peeled-off film was thoroughly washed with deionized water and then air-dried at RT. PVC thin films on a silicon wafer were prepared as follows. A volume of 50 μL 3 wt % PVC−tributyl phosphate (TBP) solution (PVC: K-value 72-71, Aladdin; TBP: AR, Sinopharm Chemical Reagent) was dipped on silicon wafers (10 mm × 10 mm, pretreated with Piranha solution), followed by a spin-coating process with a spin rate of 5000 rpm for 45 s. Finally, the polymer films together with their substrates were dried at 60 °C in a vacuum oven for 12 h. Masked removed chitosan thin films on glass substrates were prepared as follows. Chitosan solution was dipped aside a PDMS mask (lines with both width and pitch distance of 10 μm) that was placed on the substrate beforehand. Capillary force allowed the polymer solution to fill up the void space of the stamp to reduce the total free energy of the system. After solvent evaporation at a temperature of 60 °C for 24 h, the PDMS stamps were carefully peeled off from the substrate. PVC and PE sheets (99% in purity; 1 mm in thickness; Shanghai Meidi Polymer Company) and Nylon fibers (99% in purity; 1 mm in thickness; Shanghai Meidi Polymer Company) were rinsed three times with alcohol and deionized water, respectively, and then used for characterization and experiments. Regenerated silk fibroin fibers (SF; from cocoons of the silkworm *Bombyx mori*) were prepared based on the standard procedure provided by Kaplan and co-workers.[59]

Adsorption of GO on the Polymeric Substrates. Polymeric substrates were first immersed in the GO dispersion (8 mg mL^{-1}) for 1 min, followed by rinsing with deionized water to wash out residual GO (Supporting Information Figure S1a). Finally, the polymeric substrates were dried under nitrogen flow before being used for characterization and mineralization. Mask removed PVC/chitosan thin films for the height measurements of superimposed GO layers (Supporting Information Figure S1c) were prepared as follows. A rectangular-shaped PDMS mask (5 mm × 10 mm) was attached to the pre-existing PVC/chitosan thin films deposited on silicon wafers (10 mm × 10 mm), covering half of the substrate. Then, 1 mL GO dispersions (8 mg mL^{-1}) were dropped on the exposed half of the substrate for 1 min. GO was rinsed off with ultrapure water afterward. Finally, the PDMS stamps were removed to expose the area without the adsorption of GO. See fabrication details in Supporting Information Figure S16a.

Deposition of the $CaCO_3$ Mineral on Polymeric Substrates. Polymeric substrates with or without GO adsorption were used for $CaCO_3$ mineralization. First, the substrates were immersed in a volume of 4 mL 20 mM aqueous $CaCl_2$ solution (AR, Sinopharm Chemical Reagent) in the presence of 0.01 g L^{-1} poly(acrylic acid) sodium salt (PAA; average $M_w = 3 \times 10^3$ g mol^{-1}, 50 wt % in water, Sigma-Aldrich). A standard gas-diffusion method based on the decomposition of $(NH_4)_2CO_3$ (AR, Sinopharm Chemical Reagent) was used for $CaCO_3$ mineralization in a sealed desiccator for a period of 48 h. Subsequently, the substrates together with the deposits were removed and rinsed with deionized water three times before storage and characterization. In comparison experiments, mineralization proceeded in the absence of PAA additives.

Mineralization on rGO-Covered Polymeric Substrates. The rGO-adsorbed PVC films were also used for mineralization studies. To obtain rGO-covered PVC films, GO-covered PVC films were immersed in a 150 mM $NaBH_4$ (AR, Sinopharm Chemical Reagent) aqueous solution for 2 h. Afterward, the films were washed with deionized water three times. XPS was used for the chemical analysis of rGO.

Mineralization of $BaCO_3$ Nanocoatings. $BaCO_3$ nanocoatings were mineralized using 20 mM $BaCl_2$ (AR, Sinopharm Chemical Reagent) solution in the presence of 0.01 g L^{-1} PAA, respectively. GO-covered PVC films were used as receiving substrates for the deposition of these mineralized nanocoatings.

Adsorption of Ca^{2+} on rGO and GO. For the preparation of rGO, lyophilized GO monoliths were immersed in a 10 mM $NaBH_4$ aqueous solution for 2 h. The monoliths were dialyzed in deionized water three times for 24 h each and lyophilized again before use. Dry rGO/GO powders 10 mg in weight were immersed in 20 mL of 20 mmol L^{-1} $CaCl_2$ aqueous solution for 30 min. After the removal of rGO/GO powders by centrifugation, Ca^{2+} concentrations were measured with a calcium selective electrode for the calculation of the adsorption of Ca^{2+} on the rGO/GO powders.

Impedance of the Growth of $CaCO_3$ Nanocoatings with Transition Metal Cations. To test whether the presence of transition metal cations could halt the formation of $CaCO_3$ nanocoatings, a growing nanocoating on GO-covered PVC for a period of 10 h was rinsed with deionized water and quickly transferred to a solution comprising 20 mM $CaCl_2$, 0.01 g L^{-1} PAA, and 20 mM $CuCl_2$/$ZnCl_2$/$NiCl_2$ (AR, Sinopharm Chemical Reagent) to continue gas-diffusion mineralization for another 12 h. Subsequently, the substrates together with the deposits were removed and rinsed with deionized water three times before storage and characterization.

Tribological Studies. For tribological studies, a Triboindenter TI-950 (Hysitron-Bruker) equipped with a 3D Omniprobe transducer (Hysitron-Bruker) and a 50 μm cono-spherical tip was used. A ramped normal load of 120 mN for a length of 600 μm and 25 s was set and used as a scratch function. The post-scratch micrographs were captured using a digital microscope (Leica DVM6) and a field emission scanning electron microscope (JSM-7500F, JEOL). The indentation elastic moduli of the samples were measured using a standard transducer with a 30 mN maximum load capacity and a cube-corner tip calibrated for the required range using a standard fused quartz sample (E = 69 GPa). The Oliver−Pharr method[60] was used to extract the elastic modulus using the recorded loading−unloading curves.

Raman Spectroscopy and Imaging. Raman spectra of polymers, GO-covered polymers, and growing $CaCO_3$ nanocoatings on GO-covered chitosan were acquired on a HORIBA XploRA Plus (France) micro-Raman system equipped with a liquid nitrogen cooling detector. To collect Raman spectra, parameters including 532 nm excitation wavelength, a ×50 microscope objective, a numerical aperture of 0.55, and a 1200 mm^{-1} grating were used to generate a resolution of ~3 cm^{-1}.

A confocal Raman microscope (alpha300 R from WITec, Germany) equipped with a 532 nm laser was used for Raman spectroscopic imaging, where 1.2, 0.6, and 2.0 mW were used for chitosan, PVC, and growing $CaCO_3$ nanocoatings on GO-covered polymeric substrates, respectively. The microscope objective used for the spectroscopic imaging of GO-covered chitosan and PVC was ×100 (0.90 NA). The surface was scanned using 200 nm steps, and full spectra for each pixel were acquired (1 and 3 s integration times for chitosan and PVC, respectively). The microscope objective used for mapping images of growing $CaCO_3$ nanocoatings on GO-covered chitosan was ×20 (0.4 NA). The surface was scanned using 1 μm steps, and full spectra for each pixel were acquired (10 s integration time). A front illumination electron-multiplying charge-coupled device (DU970-FI from Andor) was placed behind a grating (600 mm^{-1}) spectrograph with a spectral resolution of ~3 cm^{-1}.

The WITec Control FOUR (version 4.0, WITec) and WITec Project Five (version 5.2, Plus Version, WITec) were used for measurements and data analyses, respectively. The GO images were generated by integrating the intensity of the signal of the wavenumber ranges of the G band (1587 cm^{-1}) after background subtraction. The calcite images were generated by integrating the intensity of the signal of the wavenumber ranges of the symmetric stretching mode of carbonate ion (ν_1, 1086 cm^{-1}). The polymorphic assignment of $CaCO_3$ was verified according to ref 61.

Confocal Laser Scanning Microscopy. A VK-X200 confocal laser scanning microscope was used to characterize the GO-covered polymeric substrates and growing $CaCO_3$ nanocoatings with a laser wavelength of 408 nm. All images were collected in the expert mode. The topographic information of the samples was analyzed as follows. The high and low locations of the samples were determined beforehand under the laser power source, where the Z-range was approximately 2 μm. The brightness of the laser was automatically set to be 7000 by the software. The Z pitch (distance between data points) was 0.16 μm under the RPD algorithm, which enabled high-precision results. The measurement mode was "transparent (film)", which measured all peaks to quantify the topographic information of transparent materials. The measurement quality was "super high definition", which denoted that

https://doi.org/10.1021/acs.chemmater.1c02868
Chem. Mater. 2021, 33, 9240−9251

the laser scanning method was "left-to-right, right-to-left". This laser scanning method was used to capture high-resolution, height, and laser-intensity images. The height analyses were performed on the software VK-analyzer, which provided profile information of straight lines on the height images.

Electron Microscopy. SEM images were captured by a Hitachi S4800 scanning electron microscope using a 5 kV acceleration voltage. First, the sample was treated with liquid nitrogen, and the fractured thin films were stuck onto a double-side conducting tape. Finally, the sample was sputtered with a layer of 8 nm platinum by using a JFC-600 sputter coater before characterization.

A focused ion beam (FIB)−TEM sample was prepared by using a Hitachi NB5000. A thin layer of SiO_2 was deposited on the sample by using gas-assisted deposition to protect the surface during milling and lift-out. The samples were polished to a final thickness of about 50−80 nm using a 50 pA current after lift-out and transferred onto the TEM grid. A JEM-2100 transmission electron microscope (200 kV) was employed to examine nanocoatings.

MD Simulation Studies. In this work, all MD simulations were performed in the *NVT* ensemble with NAMD.[62] Periodic boundary conditions were applied to all of the three directions. Atoms of the graphene and GO were fixed in all the simulations. A temperature of 298 K was maintained with only non-hydrogen atoms affected. A time step of 1 fs was used with atom coordinates saved every 20 ps. The particle mesh Ewald summation[63] was used to calculate the full-system periodic electrostatic interactions, with a cutoff of 1.2 nm for the separation of the direct and reciprocal space summation. The cutoff distance for van der Waals interaction was 1.2 nm.

The simulation box ($10.08 \times 10.22 \times 8.00$ nm^3) was constructed by a graphene/GO surface (with a size of 10.08×10.22 nm^2), ~16,200 Tip 3p water molecules, and 200 Ca^{2+}/CO_3^{2-} ion pairs (Supporting Information Figure S11). The atomic configuration of GO was obtained according to the reported DFT calculation.[64] To correctly describe interactions between Ca^{2+} and graphene, the cation−π effect was induced according to previous reports.[45,65] The CHARMM 27 AA force field[66] was applied for the graphene/GO substrate. For the force field parameters of Ca^{2+}/CO_3^{2-} and the Ca^{2+}/CO_3^{2-}−water interaction, the model developed by Shen *et al.* was used (Lennard-Jones potentials),[67] which is fitted from the Raiteri's model (Buckingham potentials).[68] To gain reliable results, 3 × 90 ns runs were carried out for both graphene and GO systems.

Additional Characterizations. A PHI Quantum-2000 XPS was used to record the XPS spectra of GO and rGO. POM images were collected by an Olympus BX53-P optical microscope equipped with polarizers. The XRD results were obtained by using an X'pert PRO, PANalytical, X-ray diffractometer equipped with Cu Kα radiation, where the diffraction patterns were generated with the instrument operation at 40 mA and 40 kV with a step size at 0.016°. AFM images were obtained using an atomic force microscope (Dimension FastScan, Bruker, USA) in ScanAsyst mode and using a SCANASYST-AIR tip to determine the size distribution and thickness of GO and the ultrastructural forms of the $CaCO_3$ nanocoatings.

Data Analysis. Data analysis and plotting were done using OriginPro software. Values are reported in mean ± SD format.

■ ASSOCIATED CONTENT

Supporting Information

The Supporting Information is available free of charge at https://pubs.acs.org/doi/10.1021/acs.chemmater.1c02868.

Schematic illustration of GO absorption showing the fabrication protocol of GO-covered polymeric substrates; AFM images and Raman map showing the size distribution and thickness of individual GO nanosheets and superimposed GO layers, respectively; time-resolved CLSM images showing the height statistics of growing $CaCO_3$ and $BaCO_3$ microdomains; Raman spectra/maps and XRD patterns showing $CaCO_3$ seeds and growing microdomains belonging to calcite; POM images showing birefringent information of $CaCO_3$ microcrystals and nanocoatings on different GO-covered polymeric substrates; SEM images showing the morphology of $CaCO_3$ microcrystals and damages caused by tribological tests on different GO-covered polymeric substrates; X-ray photoelectron spectra showing the percentage of C−C, C−O, and C═O for GO and rGO used for mineralization tests; systematic setup of MD simulations; and columnar diagram showing the indentation elastic moduli of the polymeric substrates and mineralized nanocoatings (PDF)

■ AUTHOR INFORMATION

Corresponding Authors

Zhisen Zhang − *State Key Laboratory of Marine Environmental Science, College of Materials, Department of Physics, State Key Laboratory for Physical Chemistry of Solid Surfaces, College of Chemistry and Chemical Engineering, Higher Educational Key Laboratory for Biomedical Engineering of Fujian Province, Graphene Industry and Engineering Research Institute, Xiamen University, Xiamen 361005, China*; orcid.org/0000-0002-8638-0993; Email: Zhangzs@xmu.edu.cn

Peter Fratzl − *Department of Biomaterials, Max Planck Institute of Colloids and Interfaces, 14476 Potsdam, Germany*; Email: Peter.Fratzl@mpikg.mpg.de

Shahrouz Amini − *Department of Biomaterials, Max Planck Institute of Colloids and Interfaces, 14476 Potsdam, Germany*; orcid.org/0000-0002-1928-2760; Email: Shahrouz.Amini@mpikg.mpg.de

Yuan Jiang − *State Key Laboratory of Marine Environmental Science, College of Materials, Department of Physics, State Key Laboratory for Physical Chemistry of Solid Surfaces, College of Chemistry and Chemical Engineering, Higher Educational Key Laboratory for Biomedical Engineering of Fujian Province, Graphene Industry and Engineering Research Institute, Xiamen University, Xiamen 361005, China*; Email: Yuan.Jiang@xmu.edu.cn

Authors

Zheng-Zheng Li − *State Key Laboratory of Marine Environmental Science, College of Materials, Department of Physics, State Key Laboratory for Physical Chemistry of Solid Surfaces, College of Chemistry and Chemical Engineering, Higher Educational Key Laboratory for Biomedical Engineering of Fujian Province, Graphene Industry and Engineering Research Institute, Xiamen University, Xiamen 361005, China*; orcid.org/0000-0002-0912-6334

Ming Li − *State Key Laboratory of Marine Environmental Science, College of Materials, Department of Physics, State Key Laboratory for Physical Chemistry of Solid Surfaces, College of Chemistry and Chemical Engineering, Higher Educational Key Laboratory for Biomedical Engineering of Fujian Province, Graphene Industry and Engineering Research Institute, Xiamen University, Xiamen 361005, China*

Yu-xuan Feng − *State Key Laboratory of Marine Environmental Science, College of Materials, Department of Physics, State Key Laboratory for Physical Chemistry of Solid Surfaces, College of Chemistry and Chemical Engineering, Higher Educational Key Laboratory for Biomedical Engineering of Fujian Province, Graphene Industry and Engineering Research Institute, Xiamen University, Xiamen 361005, China*; orcid.org/0000-0003-2581-7335

https://doi.org/10.1021/acs.chemmater.1c02868
Chem. Mater. 2021, 33, 9240−9251

Yue-E Wen − *State Key Laboratory of Marine Environmental Science, College of Materials, Department of Physics, State Key Laboratory for Physical Chemistry of Solid Surfaces, College of Chemistry and Chemical Engineering, Higher Educational Key Laboratory for Biomedical Engineering of Fujian Province, Graphene Industry and Engineering Research Institute, Xiamen University, Xiamen 361005, China;* orcid.org/0000-0002-6800-5153

Qi-Qi Huang − *State Key Laboratory of Marine Environmental Science, College of Materials, Department of Physics, State Key Laboratory for Physical Chemistry of Solid Surfaces, College of Chemistry and Chemical Engineering, Higher Educational Key Laboratory for Biomedical Engineering of Fujian Province, Graphene Industry and Engineering Research Institute, Xiamen University, Xiamen 361005, China;* orcid.org/0000-0002-5249-8088

Zihao Lu − *State Key Laboratory of Marine Environmental Science, College of Materials, Department of Physics, State Key Laboratory for Physical Chemistry of Solid Surfaces, College of Chemistry and Chemical Engineering, Higher Educational Key Laboratory for Biomedical Engineering of Fujian Province, Graphene Industry and Engineering Research Institute, Xiamen University, Xiamen 361005, China; Department of Chemistry, University of Cambridge, Cambridge CB2 1EW, U.K.*

Hua Bai − *State Key Laboratory of Marine Environmental Science, College of Materials, Department of Physics, State Key Laboratory for Physical Chemistry of Solid Surfaces, College of Chemistry and Chemical Engineering, Higher Educational Key Laboratory for Biomedical Engineering of Fujian Province, Graphene Industry and Engineering Research Institute, Xiamen University, Xiamen 361005, China;* orcid.org/0000-0001-8403-9217

Hai-Long Wang − *State Key Laboratory of Marine Environmental Science, College of Materials, Department of Physics, State Key Laboratory for Physical Chemistry of Solid Surfaces, College of Chemistry and Chemical Engineering, Higher Educational Key Laboratory for Biomedical Engineering of Fujian Province, Graphene Industry and Engineering Research Institute, Xiamen University, Xiamen 361005, China*

Bin-Bin Xu − *State Key Laboratory of Marine Environmental Science, College of Materials, Department of Physics, State Key Laboratory for Physical Chemistry of Solid Surfaces, College of Chemistry and Chemical Engineering, Higher Educational Key Laboratory for Biomedical Engineering of Fujian Province, Graphene Industry and Engineering Research Institute, Xiamen University, Xiamen 361005, China*

Helmut Cölfen − *Physical Chemistry, University of Konstanz, 78457 Konstanz, Germany;* orcid.org/0000-0002-1148-0308

Complete contact information is available at: https://pubs.acs.org/10.1021/acs.chemmater.1c02868

Author Contributions

Y.J. conceived the idea for the crystallization. P.F. and Y.J. designed mechanistic experiments. P.F. and S.A. designed and performed tribological experiments. Z.Z. performed modeling work. H.B. and M.L. synthesized and modified GO. M.L. and Y.-X.F. performed crystallization experiments. Z.-Z.L and Q.-Q.H. performed nanocoating characterization. B.-B.X. performed TEM measurements. Y-E.W. and S.A. performed confocal Raman spectroscopy measurements. H.W. and Y-E.W. performed AFM measurements. H.C. designed crystallization on variant polymers. All authors discussed results and analyzed data. Y.J., S.A., P.F., and Z.Z. drafted and revised the manuscript.

Funding

We acknowledge financial supports from the Natural Science Foundation of China (11904300, 21727807, 21875193, and 22075235) and the Fundamental Research Funds for the Central Universities (20720180066). Open access funded by Max Planck Society.

Notes

The authors declare no competing financial interest.

■ ACKNOWLEDGMENTS

We thank Profs. Song-Yuan Ding, Haiping Fang, Limin Qi, Ruikang Tang, Zhong-Qun Tian, and Shu-Hong Yu for scientific discussion and constructive comments. Siwei Li, Naibo Lin, Taoran Lin, Chuan Liu, Likun Yang, Xinxin Liu, Xinyu Liu, Yange Wang, and Xiuming Zhang are acknowledged for synthesis and characterization assistance. We acknowledge the TPK Test Center for the fabrication of FIB−TEM samples.

■ REFERENCES

(1) Dunlop, J. W. C.; Fratzl, P. Biological Composites. *Annu. Rev. Mater. Res.* **2010**, *40*, 1−24.
(2) Meyers, M. A.; McKittrick, J.; Chen, P.-Y. Structural Biological Materials: Critical Mechanics-Materials Connections. *Science* **2013**, *339*, 773−779.
(3) Meyers, M. A.; Chen, P.-Y.*Biological Materials Science: Biological Materials, Bioinspired Materials, and Biomaterials*; Cambridge University Press: Cambridge, United Kingdom, 2014.
(4) Lawn, B.*Fracture of Brittle Solids*, 2nd ed.; Cambridge University Press: Cambridge, United Kingdom, 1993.
(5) Lichtenegger, H. C.; Schöberl, T.; Bartl, M. H.; Waite, H.; Stucky, G. D. High Abrasion Resistance with Sparse Mineralization: Copper Biomineral in Worm Jaws. *Science* **2002**, *298*, 389−392.
(6) Pontin, M. G.; Moses, D. N.; Waite, J. H.; Zok, F. W. A nonmineralized approach to abrasion-resistant biomaterials. *Proc. Natl. Acad. Sci. U.S.A.* **2007**, *104*, 13559−13564.
(7) Amini, S.; Miserez, A. Wear and abrasion resistance selection maps of biological materials. *Acta Biomater.* **2013**, *9*, 7895−7907.
(8) Bentov, S.; Zaslansky, P.; Al-Sawalmih, A.; Masic, A.; Fratzl, P.; Sagi, A.; Berman, A.; Aichmayer, B. Enamel-like apatite crown covering amorphous mineral in a crayfish mandible. *Nat. Commun.* **2012**, *3*, 839.
(9) Amini, S.; Masic, A.; Bertinetti, L.; Teguh, J. S.; Herrin, J. S.; Zhu, X.; Su, H.; Miserez, A. Textured fluorapatite bonded to calcium sulphate strengthen stomatopod raptorial appendages. *Nat. Commun.* **2014**, *5*, 3187.
(10) Amini, S.; Tadayon, M.; Loke, J. J.; Kumar, A.; Kanagavel, D.; Le Ferrand, H.; Duchamp, M.; Raida, M.; Sobota, R. M.; Chen, L.; Hoon, S.; Miserez, A. A diecast mineralization process forms the tough mantis shrimp dactyl club. *Proc. Natl. Acad. Sci. U.S.A.* **2019**, *116*, 8685−8692.
(11) Erko, M.; Hartmann, M. A.; Zlotnikov, I.; Valverde Serrano, C.; Fratzl, P.; Politi, Y. Structural and mechanical properties of the arthropod cuticle: Comparison between the fang of the spider Cupiennius salei and the carapace of American lobster Homarus americanus. *J. Struct. Biol.* **2013**, *183*, 172−179.
(12) Tadayon, M.; Younes-Metzler, O.; Shelef, Y.; Zaslansky, P.; Rechels, A.; Berner, A.; Zolotoyabko, E.; Barth, F. G.; Fratzl, P.; Bar-On, B.; Politi, Y. Adaptations for Wear Resistance and Damage Resilience: Micromechanics of Spider Cuticular "Tools". *Adv. Funct. Mater.* **2020**, *30*, 2000400.
(13) Bruet, B. J. F.; Song, J.; Boyce, M. C.; Ortiz, C. Materials design principles of ancient fish armour. *Nat. Mater.* **2008**, *7*, 748−756.
(14) Yang, W.; Chen, I. H.; McKittrick, J.; Meyers, M. A. Flexible Dermal Armor in Nature. *JOM* **2012**, *64*, 475−485.

(15) Cuy, J. L.; Mann, A. B.; Livi, K. J.; Teaford, M. F.; Weihs, T. P. Nanoindentation Mapping of the Mechanical Properties of Human Molar Tooth Enamel. *Arch. Oral Biol.* **2002**, *47*, 281−291.
(16) Taylor, J. D.; Layman, M. The mechanical properties of bivalve (Mollusca) shell structures. *Palaeontology* **1972**, *15*, 73−87.
(17) Sun, T.; Feng, L.; Gao, X.; Jiang, L. Bioinspired Surfaces with Special Wettability. *Acc. Chem. Res.* **2005**, *38*, 644−652.
(18) Kato, T.; Sakamoto, T.; Nishimura, T. Macromolecular Templating for the Formation of Inorganic-Organic Hybrid Structures. *MRS Bull.* **2010**, *35*, 127−132.
(19) Wong, T.-S.; Kang, S. H.; Tang, S. K. Y.; Smythe, E. J.; Hatton, B. D.; Grinthal, A.; Aizenberg, J. Bioinspired self-repairing slippery surfaces with pressure-stable omniphobicity. *Nature* **2011**, *477*, 443−447.
(20) Elsharkawy, S.; Al-Jawad, M.; Pantano, M. F.; Tejeda-Montes, E.; Mehta, K.; Jamal, H.; Agarwal, S.; Shuturminska, K.; Rice, A.; Tarakina, N. V.; Wilson, R. M.; Bushby, A. J.; Alonso, M.; Rodriguez-Cabello, J. C.; Barbieri, E.; del Río Hernández, A.; Stevens, M. M.; Pugno, N. M.; Anderson, P.; Mata, A. Protein disorder−order interplay to guide the growth of hierarchical mineralized structures. *Nat. Commun.* **2018**, *9*, 2145.
(21) Xiao, C.; Li, M.; Wang, B.; Liu, M.-F.; Shao, C.; Pan, H.; Lu, Y.; Xu, B.-B.; Li, S.; Zhan, D.; Jiang, Y.; Tang, R.; Liu, X. Y.; Cölfen, H. Total morphosynthesis of biomimetic prismatic-type $CaCO_3$ thin films. *Nat. Commun.* **2017**, *8*, 1398.
(22) Hosoda, N.; Kato, T. Thin-film formation of calcium carbonate crystals:effects of functional groups of matrix polymers. *Chem. Mater.* **2001**, *13*, 688−693.
(23) Bevelander, G.; Nakahara, H. An electron microscope study of the formation of the nacreous layer in the shell of certain bivalve molluscs. *Calcif Tissue Res.* **1969**, *3*, 84−92.
(24) Stephens, C. J.; Ladden, S. F.; Meldrum, F. C.; Christenson, H. K. Amorphous Calcium Carbonate is Stabilized in Confinement. *Adv. Funct. Mater.* **2010**, *20*, 2108−2115.
(25) Finnemore, A. S.; Scherer, M. R. J.; Langford, R.; Mahajan, S.; Ludwigs, S.; Meldrum, F. C.; Steiner, U. Nanostructured Calcite Single Crystals with Gyroid Morphologies. *Adv. Mater.* **2009**, *21*, 3928−3932.
(26) Gong, X.; Wang, Y. W.; Ihli, J.; Kim, Y. Y.; Li, S.; Walshaw, R.; Chen, L.; Meldrum, F. C. The Crystal Hotel: A Microfluidic Approach to Biomimetic Crystallization. *Adv. Mater.* **2015**, *27*, 7395−7400.
(27) Gal, A.; Wirth, R.; Kopka, J.; Fratzl, P.; Faivre, D.; Scheffel, A. Macromolecular recognition directs calcium ions to coccolith mineralization sites. *Science* **2016**, *353*, 590−593.
(28) Joshi, R. K.; Carbone, P.; Wang, F. C.; Kravets, V. G.; Su, Y.; Grigorieva, I. V.; Wu, H. A.; Geim, A. K.; Nair, R. R. Precise and Ultrafast Molecular Sieving Through Graphene Oxide Membranes. *Science* **2014**, *343*, 752−754.
(29) Cuif, J.-P.; Burghammer, M.; Chamard, V.; Dauphin, Y.; Godard, P.; Moullac, G.; Nehrke, G.; Perez-Huerta, A. Evidence of a Biological Control over Origin, Growth and End of the Calcite Prisms in the Shells of Pinctada margaritifera (Pelecypod, Pterioidea). *Minerals* **2014**, *4*, 815−834.
(30) Elhadj, S.; De Yoreo, J. J.; Hoyer, J. R.; Dove, P. M. Role of molecular charge and hydrophilicity in regulating the kinetics of crystal growth. *Proc. Natl. Acad. Sci. U.S.A.* **2006**, *103*, 19237−19242.
(31) Huang, Q.-Q.; Wen, Y.-E.; Bai, H.; Zhang, Z.; Jiang, Y. Spontaneous Adsorption of Graphene Oxide on Multiple Polymeric Surfaces. *Langmuir* **2021**, *37*, 8829−8839.
(32) Luo, C.; Zhou, L.; Chiou, K.; Huang, J. Multifunctional Graphene Hair Dye. *Chem* **2018**, *4*, 784−794.
(33) Wang, X.; Bai, H.; Jia, Y.; Zhi, L.; Qu, L.; Xu, Y.; Li, C.; Shi, G. Synthesis of $CaCO_3$/graphene composite crystals for ultra-strong structural materials. *RSC Adv.* **2012**, *2*, 2154−2160.
(34) Berman, A.; Hanson, J.; Leiserowitz, L.; Koetzle, T. F.; Weiner, S.; Addadi, L. Biological Control of Crystal Texture: A Widespread Strategy for Adapting Crystal Properties to Function. *Science* **1993**, *259*, 776−779.
(35) Nassif, N.; Pinna, N.; Gehrke, N.; Antonietti, M.; Jager, C.; Colfen, H. Amorphous layer around aragonite platelets in nacre. *Proc. Natl. Acad. Sci. U.S.A.* **2005**, *102*, 12653−12655.
(36) Nudelman, F.; Chen, H. H.; Goldberg, H. A.; Weiner, S.; Addadi, L. Spiers Memorial Lecture Lessons from biomineralization: comparing the growth strategies of mollusc shell prismatic and nacreous layers in Atrina rigida. *Faraday Discuss.* **2007**, *136*, 9−25.
(37) Gal, A.; Kahil, K.; Vidavsky, N.; DeVol, R. T.; Gilbert, P. U. P. A.; Fratzl, P.; Weiner, S.; Addadi, L. Particle Accretion Mechanism Underlies Biological Crystal Growth from an Amorphous Precursor Phase. *Adv. Funct. Mater.* **2014**, *24*, 5420−5426.
(38) De Yoreo, J. J.; Gilbert, P. U.; Sommerdijk, N. A.; Penn, R. L.; Whitelam, S.; Joester, D.; Zhang, H.; Rimer, J. D.; Navrotsky, A.; Banfield, J. F. Crystallization by Particle Attachment in Synthetic, Biogenic, and Geologic Environments. *Science* **2015**, *349*, aaa6760.
(39) Kim, Y.-Y.; Ganesan, K.; Yang, P.; Kulak, A. N.; Borukhin, S.; Pechook, S.; Ribeiro, L.; Kröger, R.; Eichhorn, S. J.; Armes, S. P.; Pokroy, B.; Meldrum, F. C. An artificial biomineral formed by incorporation of copolymer micelles in calcite crystals. *Nat. Mater.* **2011**, *10*, 890−896.
(40) Mastropietro, F.; Godard, P.; Burghammer, M.; Chevallard, C.; Daillant, J.; Duboisset, J.; Allain, M.; Guenoun, P.; Nouet, J.; Chamard, V. Revealing crystalline domains in a mollusc shell single-crystalline prism. *Nat. Mater.* **2017**, *16*, 946−952.
(41) Gao, H. J.; Ji, B. H.; Jager, I. L.; Arzt, E.; Fratzl, P. Materials become insensitive to flaws at nanoscale: Lessons from nature. *Proc. Natl. Acad. Sci. U.S.A.* **2003**, *100*, 5597−5600.
(42) Launey, M. E.; Ritchie, R. O. On the Fracture Toughness of Advanced Materials. *Adv. Mater.* **2009**, *21*, 2103−2110.
(43) Kajiyama, S.; Nishimura, T.; Sakamoto, T.; Kato, T. Aragonite Nanorods in Calcium Carbonate/Polymer Hybrids Formed through Self-Organization Processes from Amorphous Calcium Carbonate Solution. *Small* **2014**, *10*, 1634−1641.
(44) Loh, K. P.; Bao, Q.; Eda, G.; Chhowalla, M. Graphene oxide as a chemically tunable platform for optical applications. *Nat. Chem.* **2010**, *2*, 1015−1024.
(45) Shi, G.; Liu, J.; Wang, C.; Song, B.; Tu, Y.; Hu, J.; Fang, H. Ion Enrichment on the Hydrophobic Carbon-based Surface in Aqueous Salt Solutions due to Cation-π Interactions. *Sci. Rep.* **2013**, *3*, 3436.
(46) Carter, J. G.; Aller, R. C. Calcification in the bivalve periostracum. *Lethaia* **1975**, *8*, 315−320.
(47) Sun, P.; Zheng, F.; Zhu, M.; Song, Z.; Wang, K.; Zhong, M.; Wu, D.; Little, R. B.; Xu, Z.; Zhu, H. Selective trans-membrane transport of alkali and alkaline earth cations through graphene oxide membranes based on cation−π interactions. *ACS Nano* **2014**, *8*, 850−859.
(48) Nightingale, E. R. Phenomenological Theory of Ion Solvation. Effective Radii of Hydrated Ions. *J. Phys. Chem.* **1959**, *63*, 1381−1387.
(49) Raucci, M. G.; Giugliano, D.; Longo, A.; Zeppetelli, S.; Carotenuto, G.; Ambrosio, L. Comparative facile methods for preparing graphene oxide−hydroxyapatite for bone tissue engineering. *J. Tissue Eng. Regener. Med.* **2017**, *11*, 2204−2216.
(50) Bull, S. J. Failure modes in scratch adhesion testing. *Surf. Coat. Technol.* **1991**, *50*, 25−32.
(51) Johnson, K. L.*Contact Mechanics*; Cambridge University Press: London, United Kingdom, 1985.
(52) Aizenberg, J.; Black, A. J.; Whitesides, G. H. Oriented Growth of Calcite Controlled by Self-Assembled Monolayers of Functionalized Alkanethiols Supported on Gold and Silver. *J. Am. Chem. Soc.* **1999**, *121*, 4500−4509.
(53) Loste, E.; Park, R. J.; Warren, J.; Meldrum, F. C. Precipitation of calcium carbonate in confinement. *Adv. Funct. Mater.* **2004**, *14*, 1211−1220.
(54) Aizenberg, J.; Black, A. J.; Whitesides, G. M. Control of crystal nucleation by patterned self-assembled monolayers. *Nature* **1999**, *398*, 495−498.
(55) Young, J. R.; Davis, S. A.; Bown, P. R.; Mann, S. Coccolith ultrastructure and biomineralisation. *J. Struct. Biol.* **1999**, *126*, 195−215.

https://doi.org/10.1021/acs.chemmater.1c02868
Chem. Mater. 2021, 33, 9240−9251

(56) Sanchez, C.; Belleville, P.; Popall, M.; Nicole, L. Applications of advanced hybrid organic−inorganic nanomaterials: from laboratory to market. *Chem. Soc. Rev.* **2011**, *40*, 696−753.
(57) Hammond, P. T. Form and Function in Multilayer Assembly: New Applications at the Nanoscale. *Adv. Mater.* **2004**, *16*, 1271−1293.
(58) Hummers, W. S.; Offeman, R. E. Preparation of Graphitic Oxide. *J. Am. Chem. Soc.* **1958**, *80*, 1339.
(59) Rockwood, D. N.; Preda, R. C.; Yücel, T.; Wang, X.; Lovett, M. L.; Kaplan, D. L. Materials fabrication from Bombyx mori silk fibroin. *Nat. Protoc.* **2011**, *6*, 1612−1631.
(60) Oliver, W. C.; Pharr, G. M. An improved technique for determining hardness and elastic modulus using load and displacement sensing indentation experiments. *J. Mater. Res.* **1992**, *7*, 1564−1583.
(61) Wehrmeister, U.; Soldati, A. L.; Jacob, D. E.; Häger, T.; Hofmeister, W. Raman spectroscopy of synthetic, geological and biological vaterite: a Raman spectroscopic study. *J. Raman Spectrosc.* **2010**, *41*, 193−201.
(62) Phillips, J. C.; Braun, R.; Wang, W.; Gumbart, J.; Tajkhorshid, E.; Villa, E.; Chipot, C.; Skeel, R. D.; Kalé, L.; Schulten, K. Scalable molecular dynamics with NAMD. *J. Comput. Chem.* **2005**, *26*, 1781−1802.
(63) Darden, T.; York, D.; Pedersen, L. Particle mesh Ewald: An N·log(N) method for Ewald sums in large systems. *J. Chem. Phys.* **1993**, *98*, 10089−10092.
(64) Yang, J.; Shi, G.; Tu, Y.; Fang, H. High Correlation between Oxidation Loci on Graphene Oxide. *Angew. Chem., Int. Ed.* **2014**, *53*, 10190−10194.
(65) Liu, J.; Shi, G.; Guo, P.; Yang, J.; Fang, H. Blockage of Water Flow in Carbon Nanotubes by Ions Due to Interactions between Cations and Aromatic Rings. *Phys. Rev. Lett.* **2015**, *115*, 164502.
(66) MacKerell, A. D.; Bashford, D.; Bellott, M.; Dunbrack, R. L.; Evanseck, J. D.; Field, M. J.; Fischer, S.; Gao, J.; Guo, H.; Ha, S.; Joseph-McCarthy, D.; Kuchnir, L.; Kuczera, K.; Lau, F. T. K.; Mattos, C.; Michnick, S.; Ngo, T.; Nguyen, D. T.; Prodhom, B.; Reiher, W. E.; Roux, B.; Schlenkrich, M.; Smith, J. C.; Stote, R.; Straub, J.; Watanabe, M.; Wiórkiewicz-Kuczera, J.; Yin, D.; Karplus, M. All-Atom Empirical Potential for Molecular Modeling and Dynamics Studies of Proteins. *J. Phys. Chem. B* **1998**, *102*, 3586−3616.
(67) Shen, J.-W.; Li, C.; van der Vegt, N. F. A.; Peter, C. Understanding the Control of Mineralization by Polyelectrolyte Additives: Simulation of Preferential Binding to Calcite Surfaces. *J. Phys. Chem. C* **2013**, *117*, 6904−6913.
(68) Raiteri, P.; Gale, J. D.; Quigley, D.; Rodger, P. M. Derivation of an Accurate Force-Field for Simulating the Growth of Calcium Carbonate from Aqueous Solution: A New Model for the Calcite−Water Interface. *J. Phys. Chem. C* **2010**, *114*, 5997−6010.

https://doi.org/10.1021/acs.chemmater.1c02868
Chem. Mater. 2021, 33, 9240−9251